CFD STUDY OF AIR SUPPLY SYSTEM FOR COOLING OF A HYDROGEN POWERED UNMANNED SEAPLANE AND REDUCTION OF THE RESULTING DRAG

Marsano Andrea[1], Bustos Ortega Felipe[1], Santarella Giuseppe[1], Soundararajan Sanjay Ganesh[2] & Giargia Federico[1]

[1]Politecnico di Torino, Department of Aerospace Engineering, Turin, Italy
[2]Politecnico di Torino, Department of Automotive Engineering, Turin, Italy

Abstract

The increasing sustainability demands in the aviation industry have created a considerable interest in hydrogen-powered aircraft, including unmanned aerial vehicles (UAVs). This study evaluates the integration of fuel cells[5] in a long-range UAV inspired by the historic Italian seaplane S55X Savoia-Marchetti. The primary focus is on designing and implementing a passive cooling and ventilation system within the hulls housing the fuel cells. This system prevents vapor condensation and temperature fluctuations, while ensuring that vents do not intersect the waterline during taxi, takeoff, or landing. Various system layouts were examined by adjusting the size, shape, and position of both inlets and outlets to identify the most efficient configuration with minimal induced drag.

Keywords: Hydrogen Fuel Cell, CFD, Thermal Analysis.

1. Introduction

In recent years, the aerospace industry has been increasingly focusing on hydrogen-based technologies. The transition towards a hydrogen-based economy is motivated by several factors: De-Carbonization, reduction of carbon dioxide emissions, and excessive dependence on fossil fuels.[2][13] The "S55 HERA" UAV presented in this study is a flying replica based on the historic Italian seaplane S55X Savoia-Marchetti. It was entirely created and built by the S55 student team at the Politecnico di Torino using composite materials and employing innovative technologies. Until recently, the aircraft had been electrically powered. However, the team's awareness of the aforementioned issues led to the decision to consider modifying the current power generation system by installing fuel cells on board the aircraft (specifically in the two hulls), capable of providing the necessary power during the mission [6] [1]. The need to design a cooling and ventilation system arises from the challenges associated with the use of fuel cells; mainly the management of the produced water vapor and heat. If the vapor were to remain trapped inside the hull, condensation would occur, leading to a series of problems such as the weakening of the composite structures of the hulls, an increase in weight, and interference with the onboard avionics [4]. Additionally, fuel cells have to be kept under a critical value temperature to ensure the generation of electricity. Surpassing that temperature would result in failure. One way to prevent these issues is to equip the hull with inlet and outlet holes capable of generating a convective flow inside. [12] Other designs and possible configurations, such as the implementation of active elements (e.g. fans and pumps) are not taken into consideration in this study due to construction and weight limitations on the assessed aircraft. Based on fluid dynamic analysis, inlet and outlet holes were placed at the hull's pressure extremes to exploit the maximum pressure gradient.

The focus of the research presented here is to assess how performance is affected by the shape and dimensions of the holes. The various systems' designs are numerically analyzed in order to highlight the main features that influence efficiency and to propose further improvements.The main criteria for judging the reliability of a certain configuration is set on critical operational values of the fuel-cells.

2. Pre-processing

2.1 S55 Model and design selection

The UAV model utilized in this study is the S5502, which serves as the precursor to the hydrogen-powered S55 HERA currently under development. The parameters and geometries for the HERA project have been derived from empirical data gathered from tests on the S5502 prototype. Prior experimental and numerical work highlighted key factors for designing an effective cooling system, crucial for seaplane operations.

Specifically, inlets cannot be placed below the floating line to prevent water ingress, with the floating line position determined through real-life flotation tests on the S5502(Figure 1). To identify optimal inlet and outlet positions, the pressure distribution field was analyzed, pinpointing maximum and minimum pressure points to enhance passive cooling by exploiting the maximum pressure gradient (Figure 2). This study evaluates the effectiveness of this approach. The geometry was created in Solid Works, referencing the original S5502 design. The geometry was then cleaned and meshed in ANSA CFD by BETA CAE Software, known for its robustness and detailed mesh parameter definition capabilities.

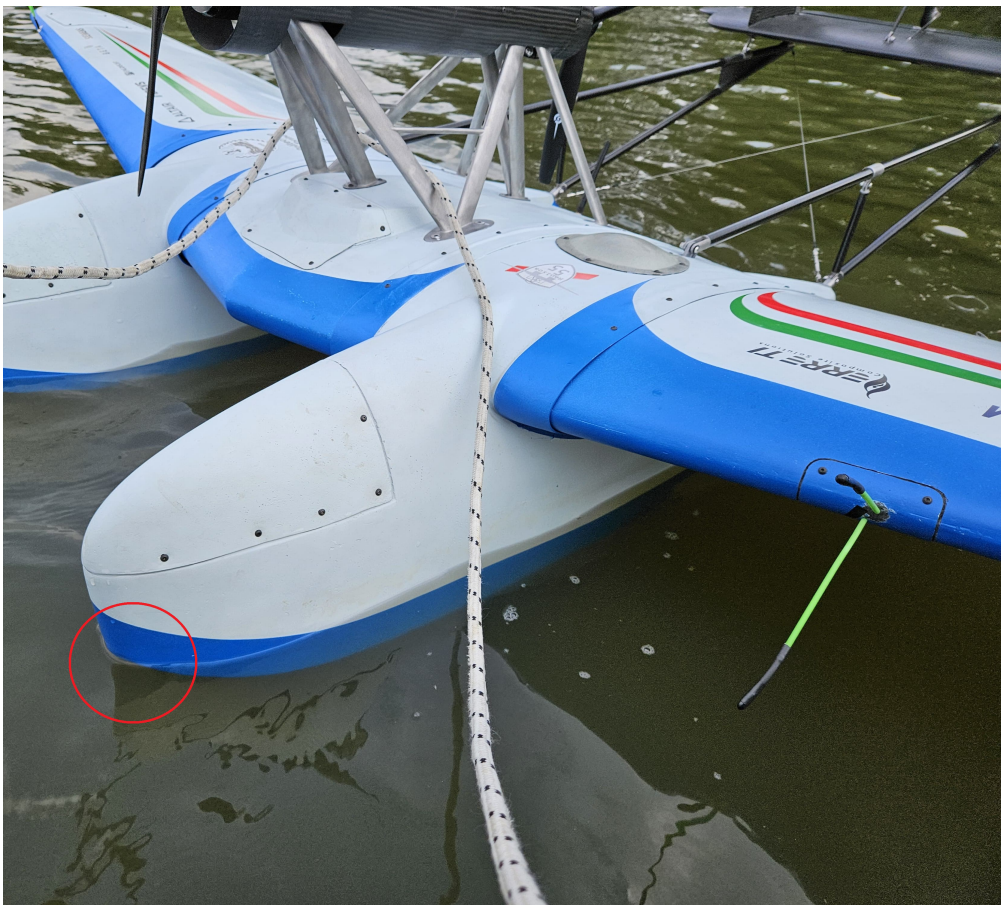

Figure 1 – Water Line

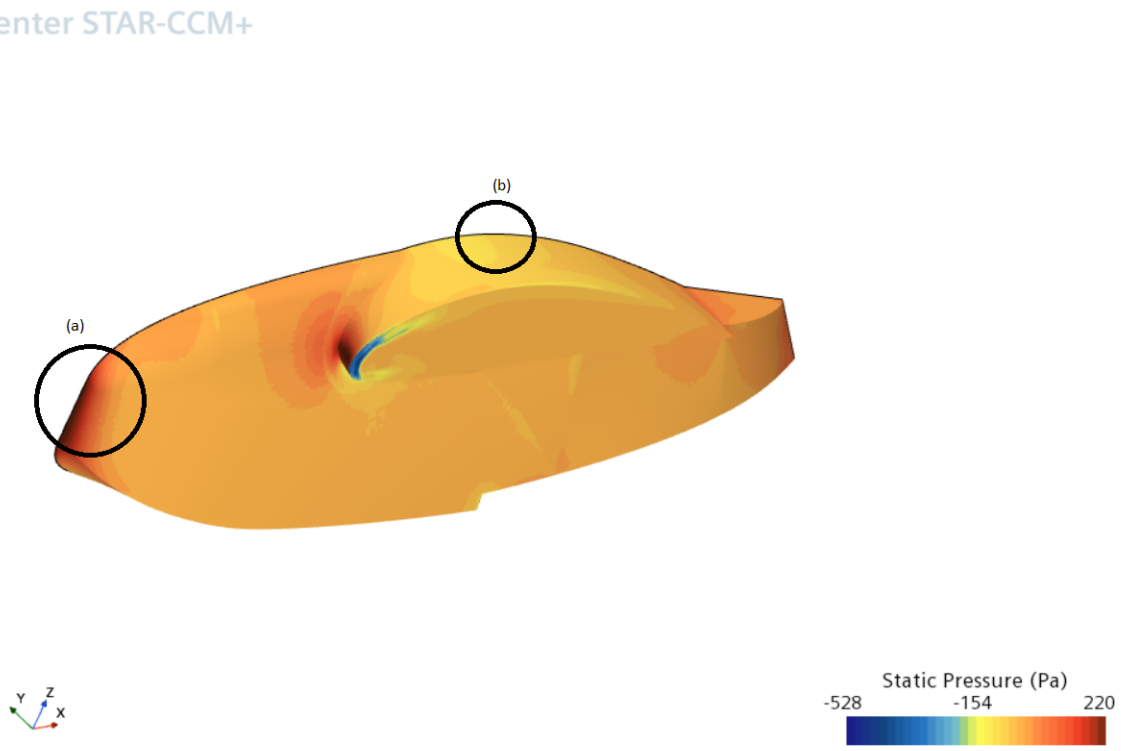

Figure 2 – Image displaying the static pressure on the surface of the hull, highlighting the maximum (a) and minimum (b) pressure areas.

2.2 Geometry and domain setup

From the CAD model of the aircraft, a completely closed geometry of the hull is derived where the holes of different shapes and sizes are placed. The aim is to determine which combination is the most aerodynamically efficient, compared to the original closed hull, denoted as "S-000". Although large inlet and outlet holes are ideal for the objectives of this study, excessive opening of the hull surface causes inevitable losses in lift and increases in drag. The many inlet and outlet combinations created and their dimensions are summarized in the Table **??**.

- **Triangular inlet - Rectangular outlet**: The isosceles triangular shape, with one of the vertices oriented downwards, has the advantage of reducing interaction between the water line and the inlet, moving much of the missing section higher. In addition, the triangular shape is the one that best fits the geometry of the hull. Nevertheless, a triangular hole is inevitably difficult to make and requires sophisticated industrial technologies. For the predominantly theoretical aims of this study, the compromise is deemed acceptable.

- **Circular inlet - Rectangular outlet**: The circular shape is the easiest to implement. As demonstrated in the literature, it allows the flow to develop uniformly inside the hull, minimizing turbulence. Starting from the point of maximum pressure, obtained during previous external flow fluid dynamics analyses, various inlet holes were created with increasing radius.

- **Rectangular inlet - Double rectangular outlet**: The rectangular inlet is the one that allows for better management of flow quantity inside the hull because it enables easy proportionality between the inlet and outlet sections. However, like the triangular shape, this form also presents certain challenges in terms of turbulence and layer overlap near the edges.

In each configuration, an inlet and a rectangular outlet with a larger area than its predecessor are featured. Nevertheless, the sides of the rectangular outlet maintain a consistent 1:2 ratio across all

geometries. The purpose of dual outlets and inlets is to explore the potential for dissipating the same volume of flow while upholding aerodynamic efficiency. The same concept is applied in some cases to increasingly bigger inlets with fixed outlets and vice-versa. Once the geometry is constructed, the domain is created. In this specific case, an orthogonal domain has been utilized, with dimensions adjusted to eliminate any interference between the hull and the walls, thus preventing simulation interruption.

Legend		
i : inlet	o : outlet	C : circular
T : triangular	R : rectangular	prefix "D" : double
prefix "t": tube	prefix "L": inlet position 1	prefix "M": inlet position 2
prefix "H": inlet position 3	suffix "L": outlet position 1	suffix "M": outlet position 2
	suffix "H": outlet position 3	

The position of the inlet is determined relative to the maximum pressure point (Figure 2). An inlet denoted by the prefix "L" is located exactly at the maximum pressure point. If the inlet has a prefix of "M" or "H", it denotes the inlet is positioned one or two centimeters above the maximum pressure point, respectively. For the outlet positioning, a suffix of "L" indicates that the outlet is at the minimum pressure point. A suffix of 2 means the outlet is four centimeters above the minimum pressure point, while a suffix of 3 indicates the outlet is four centimeters below the minimum pressure point.

2.3 Mesh

The surface mesh is obtained using first-order triangular cells . On a first-order element, the nodes are positioned at the vertices while the edges do not contain any. The triangular cell is useful and adaptable when the geometry is complex: some surfaces of the hull are very small and difficult to mesh with other types of cells (think of the internal edges of the holes). In this paper, the minimum size associated with the cells covering the hull is set to 0.4 millimeters, while the maximum size associated with the domain cells is set to 400 millimeters.

Regarding the boundary layer, it should be constructed with a structured mesh[16]. In this case, it is achieved using prismatic cells. This mesh topology is best for capturing steep gradients and any presence of viscosity. Each mesh is set up to have eight layers with an additional six outer layers added by ANSA to connect the boundary layer with the cells immediately outside. For the purposes of this study, the prismatic layer is only built on the surface of the fuel cell.Regarding the volume mesh, it is built using tetrahedral cells over the pre-existing tria surface mesh. Reminding that the mesh is different depending on the inlet and outlet sizes, nearly nine to thirteen million cells are obtained.

Table 1: Shape Configuration Dimensions.

Configuration	**Inlet sides** [*mm*]	**Outlet sides** [*mm*]
S-000	$0.0 \cdot 0.0 \cdot 0.0$	$0.0 \cdot 0.0$
M-Ti-Ro-H-1	$30.0 \cdot 42.0 \cdot 30.0$	$15.0 \cdot 30.0$
M-Ti-Ro-H-2	$38.0 \cdot 54.0 \cdot 38.0$	$19.0 \cdot 38.0$
M-Ti-Ro-H-3	$47.0 \cdot 66.0 \cdot 47.0$	$24.0 \cdot 48.0$
Configuration	**Inlet diameter** [*mm*]	**Outlet sides** [*mm*]
L-Ci-Ro-L-1	10.0	$6.5 \cdot 13.0$
L-Ci-Ro-L-2	20.0	$12.5 \cdot 25.0$
L-Ci-Ro-L-3	25.0	$15.5 \cdot 31.0$

Continued on next page

Table 1: Shape Configuration Dimensions. (Continued)

L-Ci-Ro-L-4	30.0	18.5 · 37.0
L-Ci-Ro-L-5	35.0	22.0 · 25.0
L-Ci-Ro-L-6	40.0	25.0 · 50.0
L-Ci-Ro-L-7	50.0	31.5 · 63.0
L-Ci-Ro-H-1	20.0	12.5 · 25.0
L-Ci-Ro-H-2	22.0	14.0 · 28.0
L-Ci-Ro-H-3	25.0	15.5 · 31.0
L-Ci-Ro-H-4	60.0	37.5 · 75.0
M-Ci-Ro-H-1	25.0	15.5 · 31.0
M-Ci-Ro-H-2	27.5	17.5 · 35.0
M-Ci-Ro-H-3	35.0	22.0 · 44.0
M-Ci-Ro-H-4	40.0	25.0 · 50.0
M-Ci-Ro-H-5	100.0	62.5 · 125.0
Configuration	**Inlet sides** [*mm*]	**Outlet sides of each rectangle** [*mm*]
M-Ri-DRo-M-1	27.0 · 14.0	13.5 · 14.0
M-Ri-DRo-M-2	36.5 · 19.0	18.0 · 19.0
M-Ri-DRo-M-3	46.0 · 24.0	23.0 · 24.0
M-Ri-DRo-M-4	55.5 · 29.0	27.5 · 29.0
Configuration	**Diameter of each inlet** [*mm*]	**Outlet sides** [*mm*]
L-DCi-Ro-L-1	8.0	7.0 · 14.0
L-DCi-Ro-L-2	10.0	9.0 · 18.0
L-DCi-Ro-L-3	12.5	11.0 · 21.5
L-DCi-Ro-L-4	15.0	13.0 · 27.0
L-DCi-Ro-L-5	20.0	18.0 · 35.0
Configuration	**Diameter of each inlet** [*mm*]	**Outlet sides of each rectangle** [*mm*]
L-DCi-DRo-L-1	8.0	5.0 · 10.0
L-DCi-DRo-L-2	10.0	6.0 · 13.0
L-DCi-DRo-L-3	12.5	7.5 · 16.0
Configuration	**Internal and external inlet diameter** [*mm*]	**Outlet sides** [*mm*]
L-tCi-Ro-L-1	30.0 / 30.0	18.5 · 37.0
L-tCi-Ro-M-1	20 / 25.0	28.0 · 56.0
L-tCi-Ro-H-1	15.0 / 15.0	9.5 · 19.0
L-tCi-Ro-H-2	20.0 / 15.0	11.0 · 22.0
M-tCi-Ro-L-1	15.0 / 15.0	9.5 · 19.0
M-tCi-Ro-L-2	30.0 / 30.0	18.5 · 37.0
M-tCi-Ro-L-3	35.0 / 35.0	22.5 · 45.0

Continued on next page

Table 1: Shape Configuration Dimensions. (Continued)

M-tCi-Ro-M-1	15.0 / 20.0	24.0 · 48.0
M-tCi-Ro-M-2	20.0 / 25.0	28.0 · 56.0
M-tCi-Ro-M-3	25.0 / 30.0	34.0 · 68.0
M-tCi-Ro-H-1	20.0 / 15.0	11.0 · 22.0
M-tCi-Ro-H-2	30.0 / 25.0	17.0 · 34.0
H-tCi-Ro-L-1	20.0 / 20.0	12.5 · 25.0
H-tCi-Ro-L-2	30.0 / 30.0	18.5 · 37.0
H-tCi-Ro-L-3	35.0 / 35.0	24.5 · 45.0
H-tCi-Ro-L-4	40.0 / 40.0	25.0 · 50.0
Configuration	**Internal and external diameter of each inlet** [*mm*]	**Outlet sides** [*mm*]
L-t-DCi-Ro-L-1	20.0 / 8.0	12.5 · 25.0
L-t-DCi-Ro-L-2	20.0 / 12.5	14.0 · 28.0
L-t-DCi-Ro-L-3	20.0 / 15.0	16.0 · 31.0

3. Solver setup

3.1 Turbulence model: Shear Stress Transport (SST) k-ω model

The k-ω and k-ε models are extensively utilized for closing Reynolds-Averaged Navier-Stokes (RANS) equations [15][11]

$$\frac{\partial \overline{u_i}}{\partial x_i} = 0 \tag{1}$$

$$\frac{\partial \overline{u_i}}{\partial t} + \overline{u_j}\frac{\partial \overline{u_i}}{\partial x_j} = -\frac{1}{\rho}\frac{\partial \overline{p}}{\partial x_i} + \nu\frac{\partial^2 \overline{u_i}}{\partial x_j^2} - \frac{\partial \overline{u_i' u_j'}}{\partial x_j} \tag{2}$$

enabling the practical simulation of turbulent flows by computing turbulent viscosity through transport equations for turbulence kinetic energy (k) and a dissipation-related variable (ω for k-ω, ε for k-ε)[14]. In this study, the k-ω model has been chosen as it effectively captures viscous effects near walls and adverse pressure gradients as well, in contrast to the k-ε model that exhibits greater accuracy in free-stream regions. To address the k-ω model's sensitivity to free-stream values, the Shear Stress Transport (SST) [8] k-ω model introduces a ω transport equation with a non-conservative cross-diffusion term $(\nabla k \cdot \nabla \omega)$, derived from the ε transport equation of the Standard k-ε model. A blending function (which includes functions of wall distance) ensures the application of this term far from walls, harmonizing the k-ε model's far-field behavior with the k-ω model's near-wall performance.

3.2 Segregated vs Coupled Solver

The selection of segregated flow models exerts a substantial influence on the resolution of mass and momentum conservation equation[14]. A segregated approach in solving multi-physics models involves subdividing the problem into smaller segregated steps, which reduces memory requirements and permits sequential solving. Additionally, within this study, segregated flow models are favored over their coupled counterparts, as the latter appears redundant for incompressible fluids. When opting for a segregated flow model, selecting the appropriate Segregated Fluid Energy model becomes indispensable. Among the evaluated options, namely, Segregated Fluid Enthalpy, Segregated Fluid Isothermal, and Segregated Fluid Temperature — the latter stands out as the most suitable.

3.3 Solver algorithm: Implicit unsteady vs PISO unsteady

The very small time-step needed by the PISO algorithm [3] to remain stable led to the search for a more efficient solver. With the simulations' duration being a key factor, implicit unsteady setting has

been used as it can make simulation converge more easily [10]. After all, slightly losing accuracy in the hull portions where the fluid is stuck does not jeopardize the results in terms of vapor disposal visualization.

3.4 Gas Model: Multi-component vs multi-phase

In multi-component systems, the molecular-level miscibility of different species enables them to share a common convection velocity [9][14].
Conversely, in multi-phase systems, the miscibility among different phases occurs solely at a macroscopic scale, necessitating distinct convection velocities. The primary reason for selecting a multi-component gas model lies in the microscopic mixing potential of air and water vapor. Additional considerations include the reduced computational cost associated with the multi-component gas material model and the lack of interest in investigating the behavior of condensed water. Notably, the simulation exclusively calculates the quantity of condensed water on the walls, rendering equations of motion for immersible phases unnecessary in this context.

3.5 Interfaces

In the context of this study, it is acknowledged that the hull's interaction with the fluid flow requires clearly defined interfaces between the hull's surface and the surrounding fluid region. The interfaces are defined as means of transport of physics quantities between the two regions and can be strategically utilized to effectively accommodate interactions between the various phases—namely, the gaseous phase, liquid phase, and hull walls. The interface delineating the gaseous region and the fluid film constitutes the place where condensation occurs. As shown in the table below, the creation of a shell region will automatically generate two interfaces. This ensures the virtual constant presence of a liquid region, or fluid film, between the walls and the air, characterized by a thickness that fluctuates in accordance with the condensation/evaporation rate.

gaseous region
interface
shell (i.e. fluid film)
interface
solid region

3.6 Antoine equation

To include humidity in the calculations, specific humidity q has been chosen as the best parameter to define humidity properly.

$$q = \frac{m_v}{m_v + m_d} = \frac{r}{1+r} \tag{3}$$

where m_d is the mass of dry air, m_v is the mass of water vapor, r is the mixing ratio (defined as m_v/m_d). r can be found as

$$r = \frac{0.622 \cdot P}{p_{atm} - P} \tag{4}$$

with P being the vapor equilibrium pressure.
Under particular conditions, for instance, in near-wall low-speed or low-temperature flow, this water vapor can condense into liquid water.
The phenomenon starts as soon as the partial pressure of steam in the fluid becomes greater than the saturation vapor pressure. The latter can be expressed by the Antoine equation [9]. It is an empirical relationship generally expressed as:

$$\ln\left(\frac{P}{p_{atm}}\right) = A - \frac{B}{T+C} \tag{5}$$

where P is the vapor pressure, T is the temperature, and A, B, and C are specific coefficients determined experimentally and vary from substance to substance. For the water they are: $A = 11.949$, $B = 3978.205$, $C = -39.801$. [14]

3.7 Forced convection assumptions

A multi-component solver can be computationally expensive. In order to limit the model complexity, the gravity term in the full Navier-Stokes equations might be neglected. The prevalence of forced convection over natural convection resulting from gravity can be quantified by the Richardson number

$$Ri = \frac{g \cdot \beta \cdot \Delta T_{\max} \cdot L}{U^2} \tag{6}$$

, the thermal expansion coefficient is evaluated for moist air and $T = 55°C$, resulting in $\beta = 6.6 \cdot 10^{-3}\ K^{-1}$. Similarly, the maximum $\Delta T = T_{max} - T_{ref}$ is experienced at the fuel cell, where $T = T_{max} = 57°C$. Considering the characteristic length, in a pipe flow case it would be identified as the hydraulic diameter. To keep a conservative estimation, $L = 10\ cm$ is assumed. With the discussed parameters and $g = 9.81\ m/s^2$, the local flow minimum velocity to fulfill the $Ri < 0.1$ condition is $V_{min} = 1.49 m/s$.

3.8 Boundary Conditions

S.No	Domain Initial Boundary Conditions	Values
1	Pressure	$101325.0\ Pa$
S.No	**Inlet Flow Boundary Conditions**	**Values**
1	Velocity	$20\ m/s$
2	Temperature	$293\ K$
3	Mass Fraction	[1:0] ([Air:Steam])
3	Air Specific Heat	$1003.62\ J/(kg \cdot K)$
4	Air Dynamic Viscosity	$1.85508 \cdot 10^{-5} Pa \cdot s$
S.No	**Fuel Cell Steam Boundary Conditions**	**Values**
1	Mass Flow Rate	$7.0 \cdot 10^{-4}\ kg/s$
2	Temperature	$327.0\ K$
3	Mass Fraction	[0:1] ([Air:Steam])
4	Specific Heat	$1938.19\ J/(kg \cdot K)$
5	Dynamic Viscosity	$1.26765 \cdot 10^{-5}\ Pa \cdot s$

Table 2 – Boundary Conditions

4. Result analysis

4.1 Quality Criteria, Residual and Predetermined Checks

A series of quality criteria have been imposed in order to preliminary discard and expose inefficient configurations. These indicators are obtained from real-life practical limitations. Critical fuel cell temperature is regarded as a determining factor to assess the validity of a certain geometry [4]. Simulations that display temperature above this value are rejected. Additionally, the amount of condensed water inside the hull must be kept below (insert value) as to prevent detrimental liquid buildup. For this reason, the condensation layer thickness is also a crucial evaluation criterion. Velocity and pressure field distribution are also consulted to verify the reliability of the simulated results. These parameters are taken into account only if the examined simulation has converged and thus the numerical result evaluated is accurate.

4.2 Velocity Profile

Velocity profiles in the Simulation are created with a plane running along the length of the plane, parallel to the flow of air. This helps us understand the flow inside the hull. In certain configurations,

the flow of air is non-deviating and comparatively linear (Figure 3(a)). This represents a configuration with desirable flow. However, certain configurations do not have any airflow into the hull (Figure 4(b)).

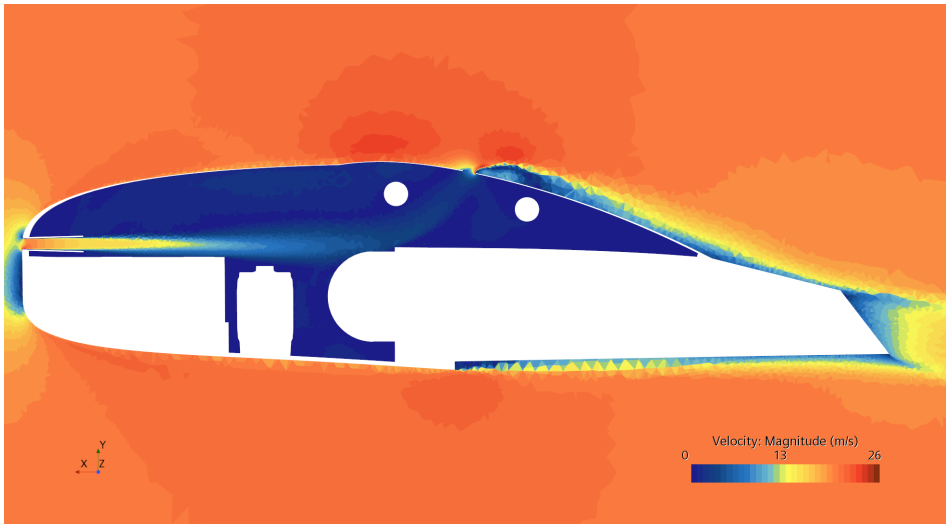

Figure 3 – (a) Velocity Scene

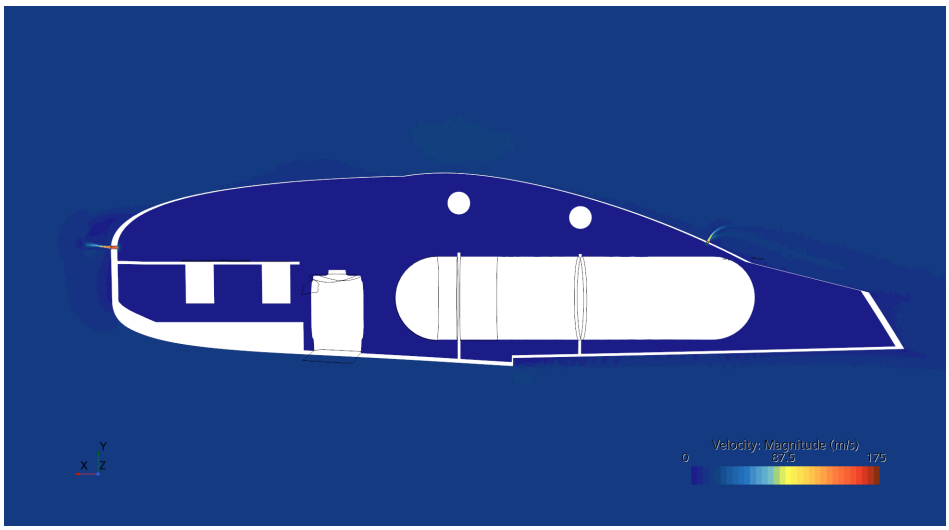

Figure 4 – (b) Velocity Scene

4.3 Temperature Profile

Similar to the velocity profile, a plane that runs parallel to the flow of air is created. In more desirable simulations, the temperature around the fuel cell is below the critical working temperature (Figure 5(a)). However, in the case of the simulations diverging, this often caused radical changes in temperature which led to failure due to the temperature exceeding the critical temperature of the fuel cell (Figure 6(b)).

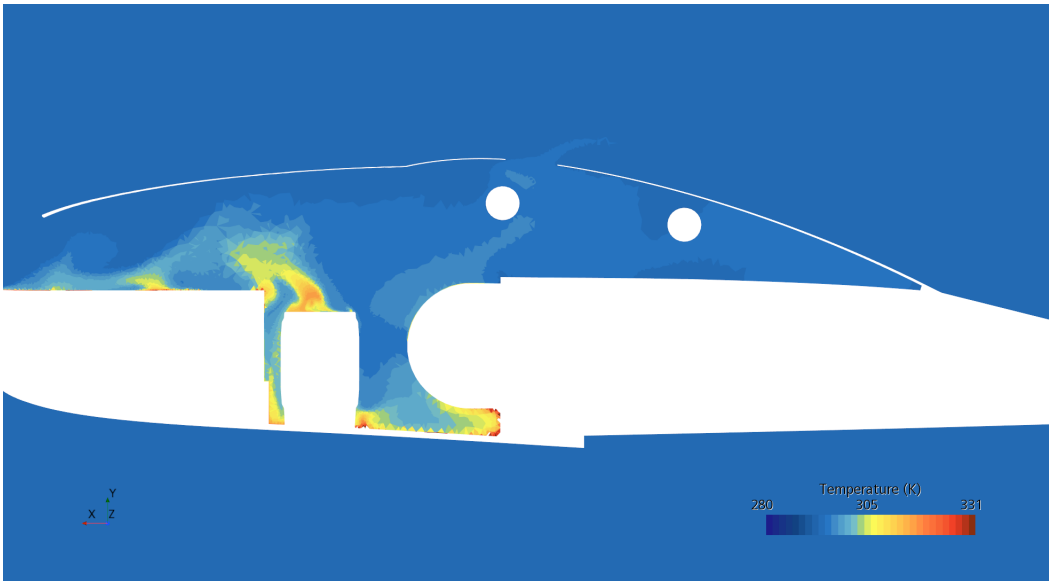

Figure 5 – (a) Temperature Scene

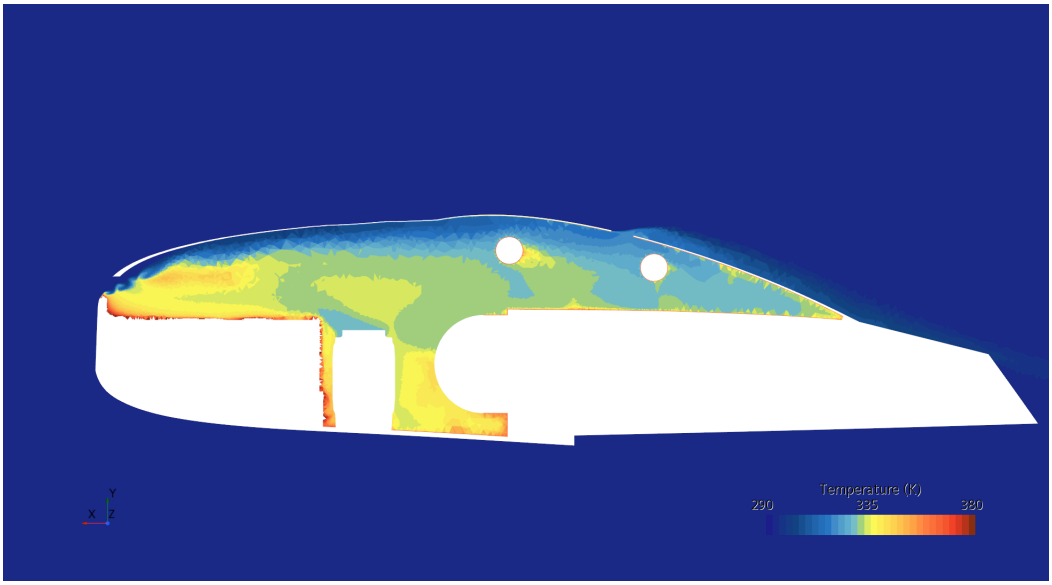

Figure 6 – (b) Temperature Scene

4.4 Mass Fraction Profile and water thickness

Mass fraction profiles denote the presence of water in the air. This helps one pinpoint the presence of steam. A good quality simulation has a lower concentration of H_2O Mass Fraction inside the hull (Figure 7(a)), whereas a poor configuration may yield a hull that is completely filled with steam (Figure 8(b)). Considering that the model S55-HERA is intended to fly for approximately 200 km, it is crucial to minimize the presence of water. As for the simulations displayed in table 3, considering a 3-hour flight, the aim is for a near-zero thickness of the water layer. To ensure the correct ventilation of S55-HERA, the water layer must not exceed $1 \cdot 10^{-7} m$. However, a thickness closer to the $1 \cdot 10^{-6} m$ mark is more desirable as, throughout the full flight, less than 0.5 mm of water would be accumulated inside the hulls. In this study, any configuration that fails to fulfill this requisite or displays a divergence in temperature will present the wording "inf" in the water layer thickness (Figure 3, indicating a potentially infinite amount of water as the physical time of the simulation increases.

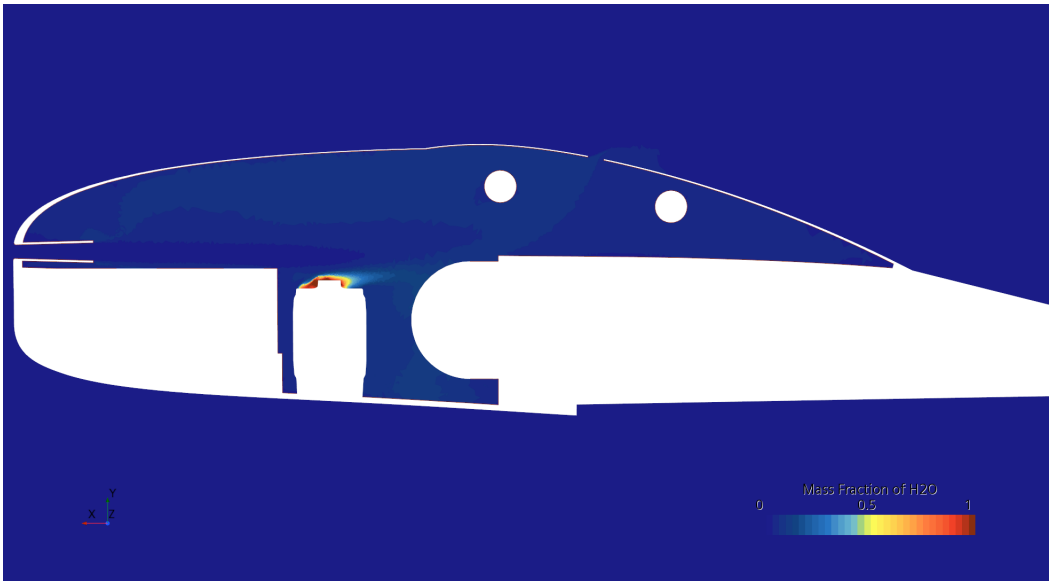

Figure 7 – (a) Mass Fraction of $H20$

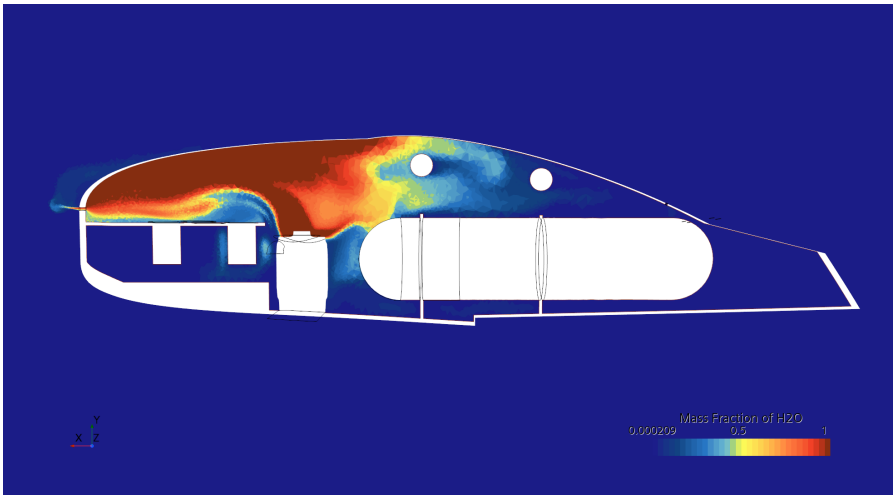

Figure 8 – (b) Mass Fraction of $H20$

4.5 Residuals

Good quality simulations do not only depend on the visual results they produce, but also on the convergence of the residuals. An acceptable limit for residual convergence is 10^{-2} or below (Figure 9).

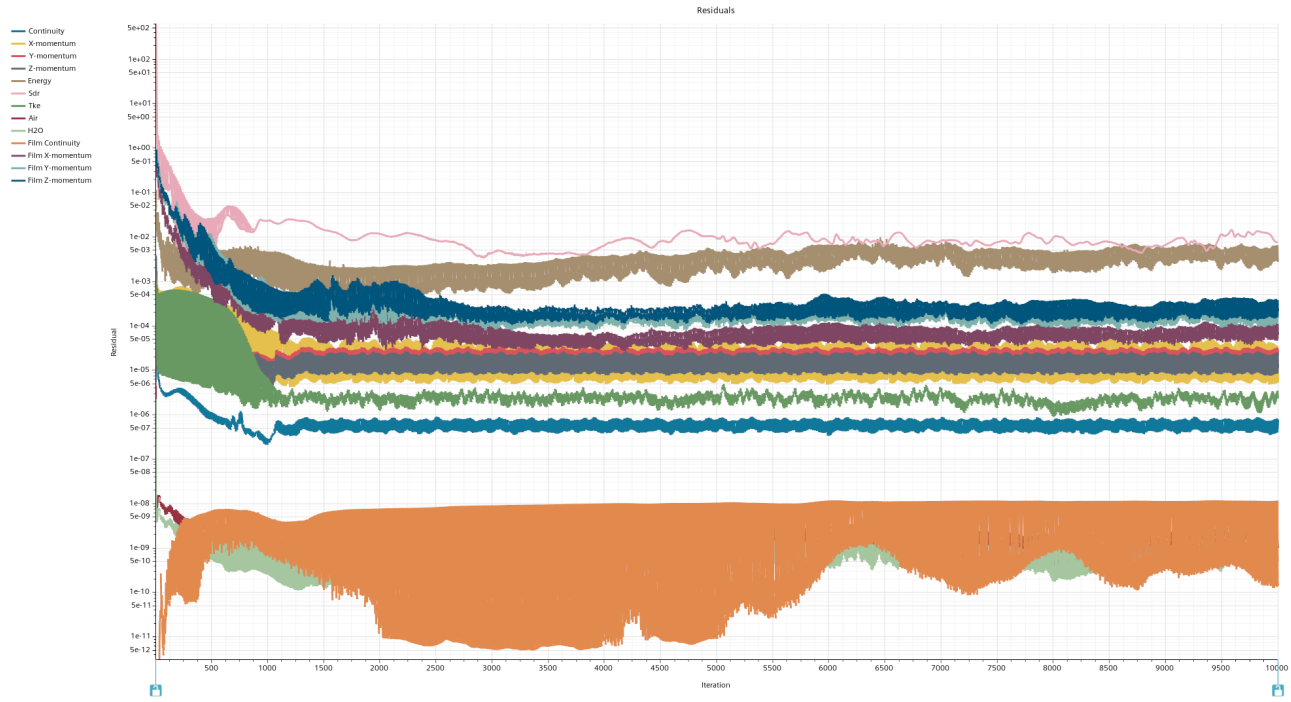

Figure 9 – Residuals.

4.6 Velocity Probes

To account for the flow along the top of the hull and the flow beyond the fuel cell, two virtual probes were created. These probes recorded data regarding the velocity of the flow at that particular point. Probe 1 Is placed directly behind the fuel cell steam stack. The second probe is placed higher along the flow path of most flow paths (Figure 10).

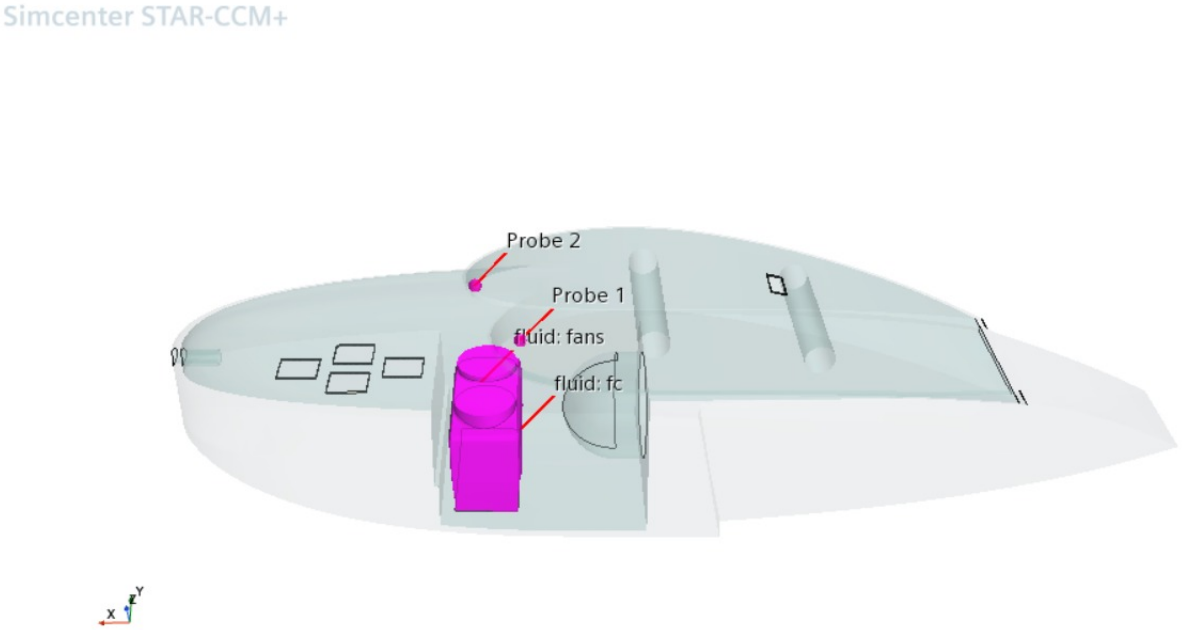

Figure 10 – Probe Locations

Simulation	**Probe 1 Velocity** [*m/s*]	**Probe 2 Velocity** [*m/s*]	C_D	**Average thickness** [*mm*]
S-000	–	–	0.0372	–
M-Ti-Ro-H-1	0.656	6.99	0.04408	inf
M-Ti-Ro-H-2	0.172	4.63	0.04329	inf
M-Ti-Ro-H-3	3.59	3.13	0.04672	$5.226 \cdot 10^{-3}$
L-Ci-Ro-L-1	0.015	0.04	0.04023	inf
L-Ci-Ro-L-2	0.023	0.054	0.04043	inf
L-Ci-Ro-L-3	0.292	5.45	0.04068	$1.03 \cdot 10^{-2}$
L-Ci-Ro-L-4	0.4	4.11	0.04183	inf
L-Ci-Ro-L-5	0.515	7.95	0.04425	$2.14 \cdot 10^{-3}$
L-Ci-Ro-L-6	3.46	3.79	0.04596	$4.4 \cdot 10^{-3}$
L-Ci-Ro-L-7	3.05	6.01	0.047	$3.40 \cdot 10^{-3}$
L-Ci-Ro-H-1	0.017	0.0535	0.0384	inf
L-Ci-Ro-H-2	0.0469	0.169	0.03958	inf
L-Ci-Ro-H-3	0.0316	0.0418	0.04008	inf
L-Ci-Ro-H-4	0.146	2.97	0.051	$3.67 \cdot 10^{-3}$
M-Ci-Ro-H-1	0.558	5.57	0.04377	$7.54 \cdot 10^{-3}$
M-Ci-Ro-H-2	5.31	1.3	0.0453	$9.00 \cdot 10^{-3}$
M-Ci-Ro-H-3	2.24	10.3	0.04681	$8.00 \cdot 10^{-3}$
M-Ci-Ro-H-4	1.37	7.74	0.04933	$4.66 \cdot 10^{-3}$
M-Ci-Ro-H-5	2.38	9.27	0.05876	$4.23 \cdot 10^{-4}$
M-Ri-DRo-M-1	0.102	0.0661	0.04037	inf
M-Ri-DRo-M-2	0.471	4.28	0.04171	inf
M-Ri-DRo-M-3	0.381	6.2	0.04205	inf
M-Ri-DRo-M-4	0.339	8.17	0.04297	inf
L-DCi-Ro-L-1	0.312	0.0425	0.04021	inf
L-DCi-Ro-L-2	0.04	0.224	0.04017	inf
L-DCi-Ro-L-3	0.0381	0.0633	0.04042	inf
L-DCi-Ro-L-4	0.0647	0.126	0.04019	inf
L-DCi-Ro-L-5	0.204	0.482	0.04066	$5.31 \cdot 10^{-2}$
L-DCi-DRo-L-1	0.7	0.2	0.03917	inf
L-DCi-DRo-L-2	0.161	0.545	0.04048	inf
L-DCi-DRo-L-3	0.7	0.3	0.04068	$4.98 \cdot 10^{-2}$
L-tCi-Ro-L-1	0.2	0.66	0.04024	$8.1 \cdot 10^{-3}$
L-tCi-Ro-M-1	4.89	1.05	0.04265	$3.301 \cdot 10^{-3}$
L-tCi-Ro-H-1	0.938	0.781	0.04053	inf
L-tCi-Ro-H-2	1.71	0.9	0.04074	$4.03 \cdot 10^{-3}$
M-tCi-Ro-L-1	0.005	0.01	0.04026	inf
M-tCi-Ro-L-2	0.6	2.45	0.04219	inf
M-tCi-Ro-L-3	0.508	5.19	0.04203	inf
M-tCi-Ro-M-1	3.93	1.8	0.04163	$4.63 \cdot 10^{-3}$
M-tCi-Ro-M-2	4.17	1.6	0.0418	$3.76 \cdot 10^{-3}$
M-tCi-Ro-M-3	4.49	1.48	0.04208	$2.63 \cdot 10^{-3}$
M-tCi-Ro-H-1	0.768	0.611	0.04066	inf
M-tCi-Ro-H-2	3.52	1.56	0.04111	$5.30 \cdot 10^{-3}$
H-tCi-Ro-L-1	0.372	3.16	0.04089	inf
H-tCi-Ro-L-2	3.44	1.33	0.04314	$4.00 \cdot 10^{-3}$
H-tCi-Ro-L-3	1.12	4.83	0.04314	inf
H-tCi-Ro-L-4	0.653	5.02	0.04224	$2.80 \cdot 10^{-3}$
L-t-DCi-Ro-L-1	0.02	0.05	0.04038	$1.46 \cdot 10^{-2}$
L-t-DCi-Ro-L-2	1.4	0.5	0.04075	$3.33 \cdot 10^{-3}$
L-t-DCi-Ro-L-3	2	0.6	0.04119	$2.30 \cdot 10^{-3}$

Table 3 – Results database

5. Result inference

The initial configurations denote a perfectly rectangular (Figure 14) shape imposed onto the front surface of the plane. This was later followed by configurations with triangular (Figure 11)inlet. These configurations displayed extreme turbulence on the edges and corners. This caused the inlet velocity of the air to reduce considerably. It was observed, that a higher-placed triangular or rectangular configuration allowed air to flow downwards as compared to a lower-placed inlet of the same configuration. However, it suffers from vortex generation due to turbulence, which ultimately causes back-flow and re-circulation inside the hull.

To solve the issue of the creation of vortexes and prevent the reduction of flow velocity, circular inlets were created. This configuration was observed to have drastic improvements in vortex reduction. However, further studying the placement of this configuration in conjunction with different outlet placements and sizes revealed interesting information regarding flow improvement factors.

Initially, a small inlet was created along with an outlet placed in the back of the hull. This configuration was intended to eliminate the flow deviation, thus reducing the induced turbulence. However, as many of the results of table 3 highlight, it prevented adequate airflow through the inlet. This led the steam generated by the fuel cell to build up and caused critical failure in operational temperature for the fuel cell.

To aid in increasing the inflow of air through the inlet, much larger inlet and outlet shapes were created (Figure 15). However, this caused a slew of issues, both aerodynamic and thermal [7]. Due to an excessively large inlet, the obtained coefficient of drag was considerably higher. Moreover, as the velocities along the two probes display, the flow of air was always deviated upwards by the air near the stagnation point, partially avoiding the steam being generated.

The creation of the outlet over the maximum pressure differential zone (Figure 16) caused air to be sucked out of the hull. This aided in increasing the flow rate. However, especially if paired with a smaller inlet, the minimum velocity criterion was not satisfied. Applying the same methodology as the previous configuration, the inlet and outlet sizes were increased.

To confront the flow of air along the top of the hull, a fillet was created on the lip of every circular inlet. This proved to be beneficial as it redirected the flow closer to the fuel cell height. After achieving the first admissible configurations, with a water layer thickness of less than $1 \cdot 10^{-7} m$ after convergence, an in-depth analysis of the drag reduction began, while still keeping proper ventilation along the hulls. In this regard, although a very large hole would be beneficial for the reduction of the water-to-air ratio, it would be detrimental to the aerodynamics. To further improve the airflow, a small compression tube was created (Figure 13). The addition allowed the air to be directed very accurately toward the maximum humidity area. This also prevented the turbulent air coming from the inlet from dispersing and recirculating. The position of the created inlet for the tube configuration was extremely critical. An inlet created close to the bottom, paired with an outlet on the extreme end of the hull (Figure 12) often caused the flow of air to carry the generated steam over the tank, where it would condense. Over larger periods of time, the water layer thickness would eventually rise above the chosen tolerance. To solve this problem, the same inlet paired with an outlet over the maximum pressure differential region meant that the generated steam would be carried away directly into the outlet without condensing over the tank.

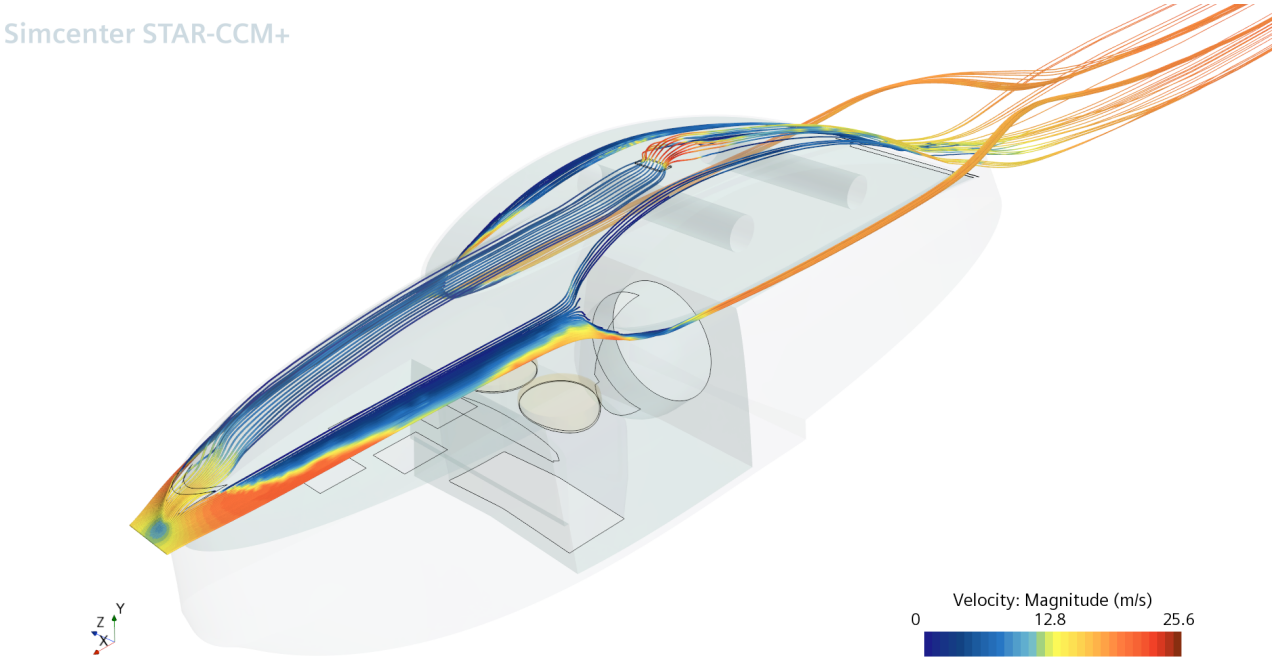

Figure 11 – Triangle Inlet Velocity Streamline.

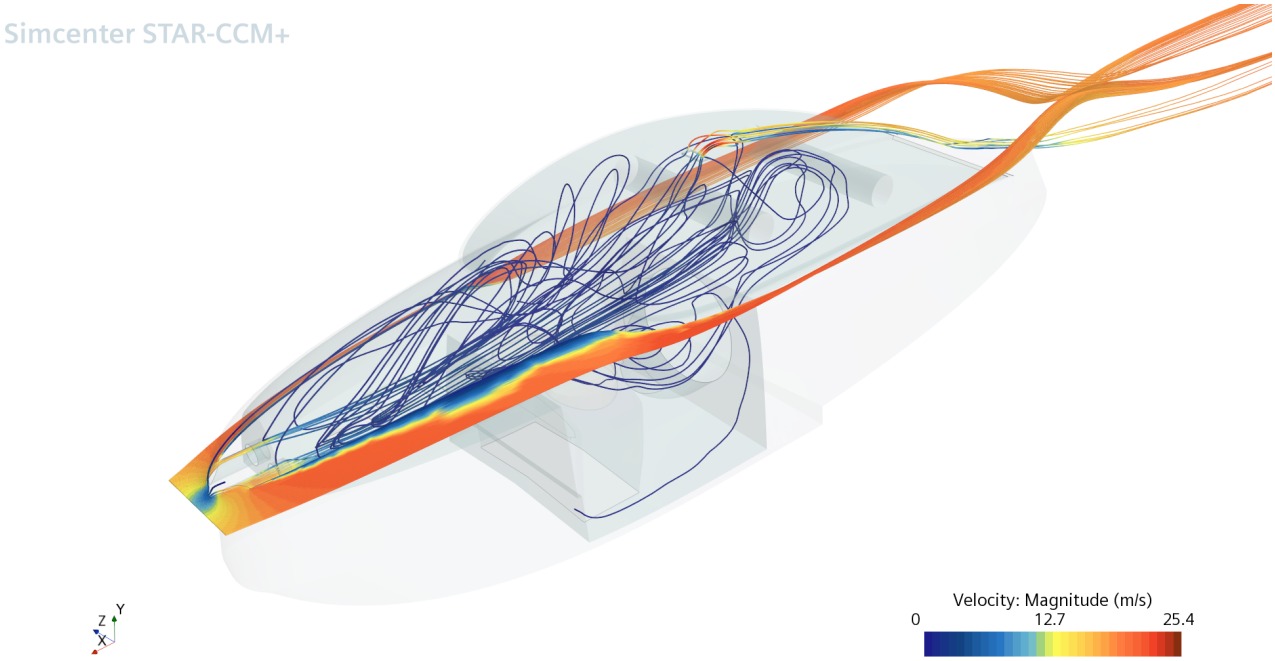

Figure 12 – Double Inlet Tube Velocity Streamline.

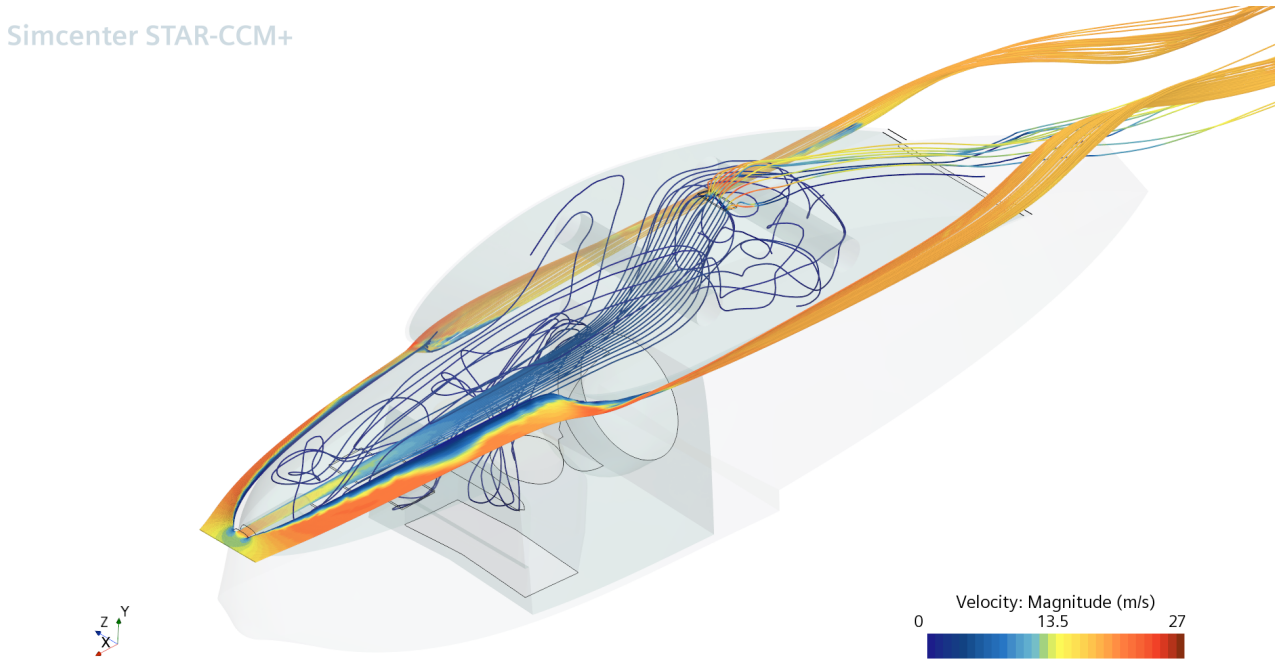

Figure 13 – Single Inlet Tube Velocity Streamline.

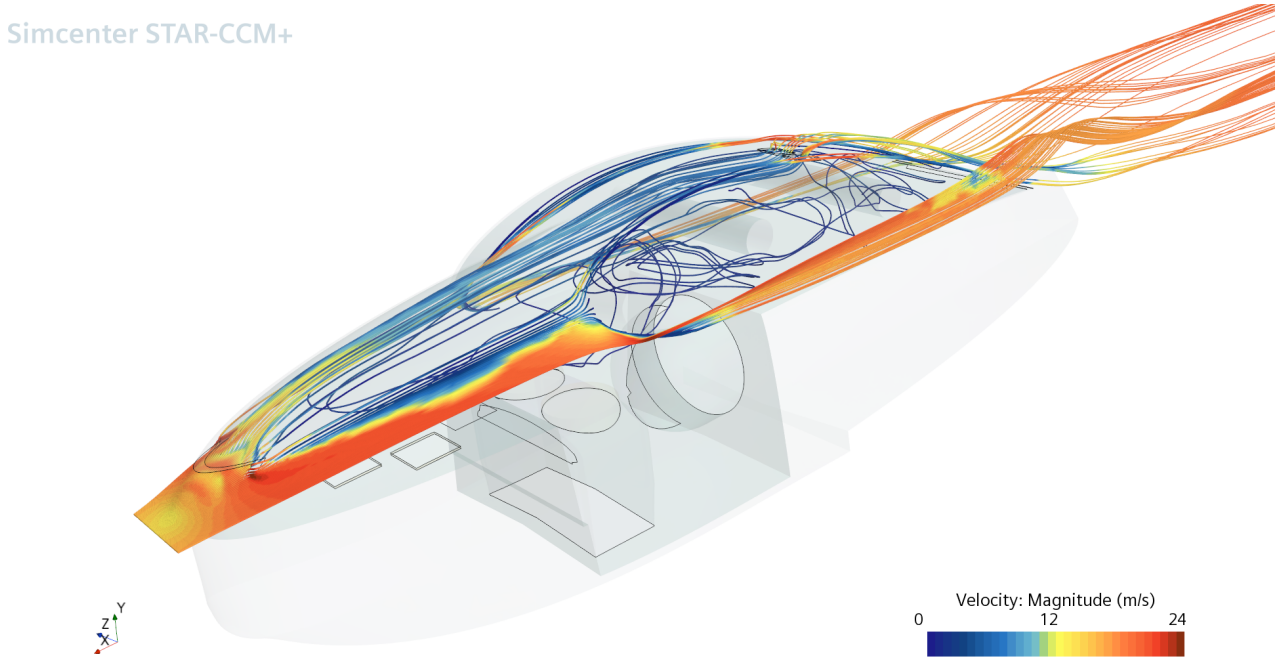

Figure 14 – Rectangular Inlet Velocity Streamline.

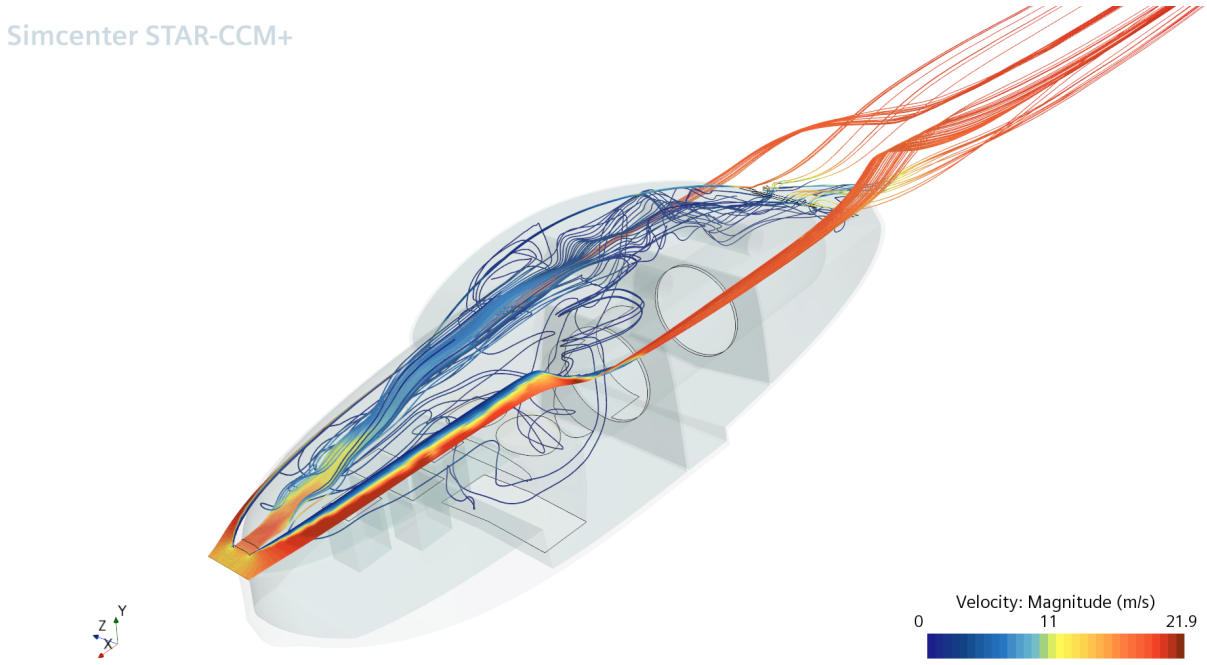

Figure 15 – Circle Rear Outlet Velocity Streamline.

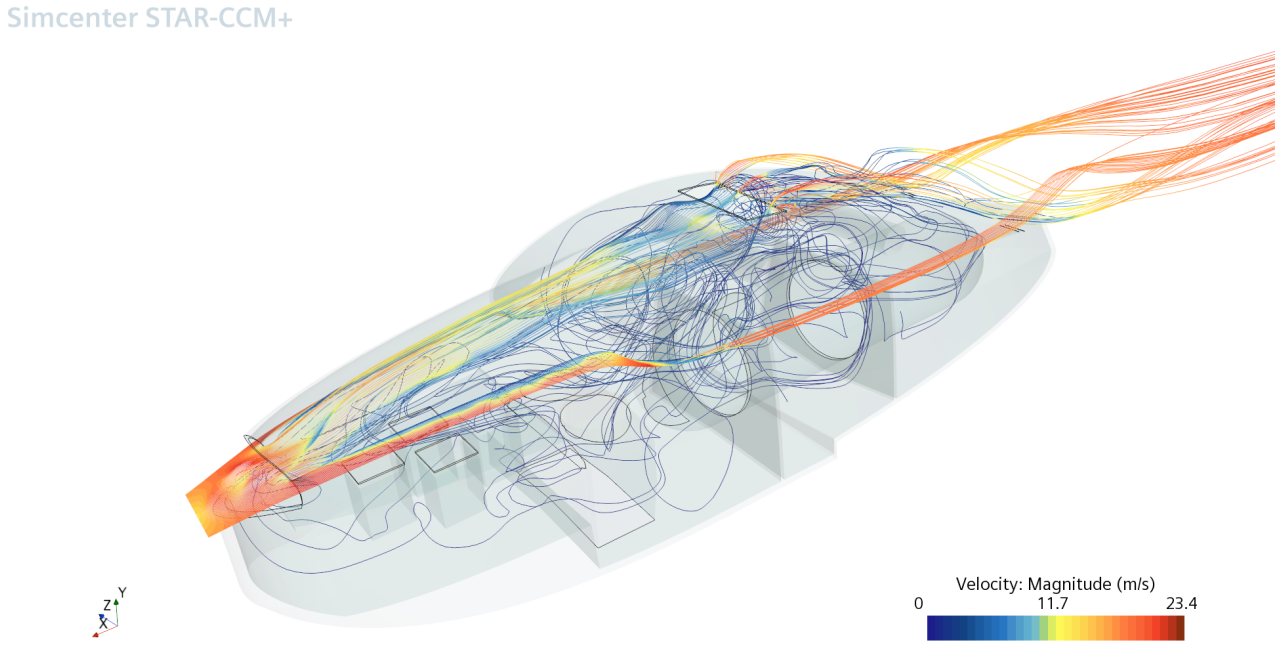

Figure 16 – Circle Min. Pressure Outlet Velocity Streamline.

6. Conclusions

In this study, various shape configurations were tested to evaluate their impact on drag and internal temperature management. Configurations with large inlets and outlets consistently resulted in significantly higher drag, which contradicts the primary goal of our paper. Conversely, configurations with smaller inlets and outlets failed to sufficiently reduce the internal temperature of the hull due to restricted airflow. Ultimately, configurations with moderately sized inlets and outlets were found to be optimal, as they provide a balanced solution to both reducing drag and maintaining effective thermal management.

The investigation revealed that shape configurations featuring sharp edges tended to induce turbu-

lence. This challenge was mitigated by either chamfering or filleting the edges, resulting in a notable reduction of turbulence generation. Additionally, it was noted that certain configurations, due to the pressure disparity between the lower and upper halves of the created inlets, caused airflow to preferentially travel along the top of the hull, neglecting the steam from the fuel cells and leading to inadequate interior cooling. To remedy this limitation, a dedicated channel was implemented to guide airflow directly over critical overheating areas. This approach emerged as the most effective strategy for cooling the fuel cell and enhancing overall performance.
As a final note, it is recommended that future research endeavors concentrate on identifying the most suitable dimensions for the tube and integrating active elements like fans. Besides, the availability of more powerful numerical calculus means precision would let to refine the time-step resolution. Further, in order to increase the accuracy of the simulation, the time step of the simulation could be reduced, which would directly lead to a better CFL number.

6.1 Acknowledgements

The authors express their gratitude to the Politecnico di Torino and the DIMEAS department for the provision of resources and facilities. We also extend our thanks to DAUIN for the computational resources provided through High-Performance Computing Polito (HPC@POLITO), a project of Academic Computing within the Department of Control and Computer Engineering at the Politecnico di Torino (http.//www.hpc.polito.it). Special thanks go to SIEMENS and BETA CAE for their support and for providing the software licenses. Heartfelt thanks also go to Professor Enrico Cestino and the entire student team "TeamS55" for the opportunity provided and for the acquired knowledge.

7. Copyright Statement

References

[1] Zhijie Duan, Nan Mei, Lili Feng, Shuguang Yu, Zengyou Jiang, Dongfang Chen, Xiaoming Xu, and Jichao Hong. Research on hydrogen consumption and driving range of hydrogen fuel cell vehicle under the cltc-p condition. *World Electric Vehicle Journal*, 13(1):9, 2021.

[2] Pobitra Halder, Meisam Babaie, Farhad Salek, Kalpit Shah, Svetlana Stevanovic, Timothy A Bodisco, and Ali Zare. Performance, emissions and economic analyses of hydrogen fuel cell vehicles. *Renewable and Sustainable Energy Reviews*, 199:114543, 2024.

[3] Raad I Issa. Solution of the implicitly discretised fluid flow equations by operator-splitting. *Journal of computational physics*, 62(1):40–65, 1986.

[4] Alexander Kabza. Fuel cell formulary. *Kabza, Ed*, 2015.

[5] Kyunghwan Kim, Taegyu Kim, Kiseong Lee, and Sejin Kwon. Fuel cell system with sodium borohydride as hydrogen source for unmanned aerial vehicles. *Journal of power sources*, 196(21):9069–9075, 2011.

[6] N Lapeña-Rey, JA Blanco, E Ferreyra, JL Lemus, S Pereira, and E Serrot. A fuel cell powered unmanned aerial vehicle for low altitude surveillance missions. *International Journal of Hydrogen Energy*, 42(10):6926–6940, 2017.

[7] Francesco Larocca, Andrea Ferrero, and Marco Castiglione. Analisi del flusso viscoso all'interno di canali interpalari di turbomacchina.

[8] Florian R Menter, Martin Kuntz, Robin Langtry, et al. Ten years of industrial experience with the sst turbulence model. *Turbulence, heat and mass transfer*, 4(1):625–632, 2003.

[9] Bruce E Poling, John M Prausnitz, John P O'connell, et al. *The properties of gases and liquids*, volume 5. Mcgraw-hill New York, 2001.

[10] Alessandro Porcarelli. Development of a cfd model and methodology for the internal flow simulation in a hydrogen-powered uav, 2021.

[11] GABRIELE RIVA. Simulazione rans con schemi cinetici dettagliati di un meso-combustore in pressione. 2011.

[12] Giulio Romeo, Enrico Cestino, Fabio Borello, and G Correa. Engineering method for air-cooling design of two-seat propeller-driven aircraft powered by fuel cells. *Journal of Aerospace Engineering*, 24(1):79–88, 2011.

[13] Giulio Romeo, G Correa, Fabio Borello, Enrico Cestino, and Massimo Santarelli. Air cooling of a two-seater fuel cell–powered aircraft: Dynamic modeling and comparison with experimental data. *Journal of Aerospace Engineering*, 25(3):356–368, 2012.

[14] Siemens. *Simcenter STAR-CCM+ Documentation Version 2022.1*. 2022 Siemens Digital Industries Software, 2022.

[15] Siwat Suewatanakul, Alessandro Porcarelli, Adam Olsson, Henrik Grimler, Ariel Chiche, Raffaello Mariani, and Göran Lindbergh. Conceptual design of a hybrid hydrogen fuel cell/battery blended-wing-body unmanned aerial vehicle—an overview. *Aerospace*, 9(5):275, 2022.

[16] Henk Kaarle Versteeg. *An introduction to computational fluid dynamics the finite volume method, 2/E*. Pearson Education India, 2007.